AD_____

Award Number: W81XWH-08-1-0613

TITLE: X-Ray Phase Imaging For Breast Cancer Detection

PRINCIPAL INVESTIGATOR: Xizeng Wu, Ph.D.

CONTRACTING ORGANIZATION: University of Alabama at Birmingham,
Birmingham, AL 35294

REPORT DATE: September 2010

TYPE OF REPORT: Annual

PREPARED FOR: U.S. Army Medical Research & Materiel Command
Fort Detrick, Maryland 21702-5012

REPORT DOCUMENTATION PAGE

Form Approved
OMB No. 0704-0188

1. REPORT DATE *(DD-MM-YYYY)*	2. REPORT TYPE	3. DATES COVERED *(From - To)*
30-09-2010	Annual	01 Sep 2009 - 31 Aug 2010

4. TITLE AND SUBTITLE

X-Ray Phase Imaging For Breast Cancer Detection

5a. CONTRACT NUMBER

5b. GRANT NUMBER
W81XWH-08-1-0613

5c. PROGRAM ELEMENT NUMBER

6. AUTHOR(S)
Xizeng Wu, Ph.D.

E-Mail: xwu@uabmc.edu

5d. PROJECT NUMBER

5e. TASK NUMBER

5f. WORK UNIT NUMBER

7. PERFORMING ORGANIZATION NAME(S) AND ADDRESS(ES)

University of Alabama at Birmingham,
Birmingham, AL 35294

8. PERFORMING ORGANIZATION REPORT NUMBER

9. SPONSORING / MONITORING AGENCY NAME(S) AND ADDRESS(ES)
U.S. Army Medical Research and Material
Fort Detrick, Maryland 21702-5012

10. SPONSOR/MONITOR'S ACRONYM(S)

11. SPONSOR/MONITOR'S REPORT NUMBER(S)

12. DISTRIBUTION / AVAILABILITY STATEMENT

Approved for public release; distribution unlimited

13. SUPPLEMENTARY NOTES

14. ABSTRACT

- The long term objective of the project is to develop a low-dose and quantitative phase x-ray imaging technique for facilitating breast cancer detection. In this period we have accomplished following tasks: (1) We refined the attenuation-partition based phase retrieval method for speeding up the iteration convergence, and systematically and quantitatively compared its performance against that of the mostly used phase retrieval method (the TIE method). A digital breast lumpectomy specimen model was constructed for facilitating the quantitative evaluations. We showed that the attenuation-partition based phase retrieval method is much more robust against image noise and the alignment errors than the TIE method does. (2) The system hardware integration has been completed in this period. The tests showed that the system is functioning for phase contrast image acquisition with high energy x-rays. The efforts for technique optimization are under the way.

15. SUBJECT TERMS
Phase-contrast x-ray imaging, Breast imaging, Phase retrieval

16. SECURITY CLASSIFICATION OF:			17. LIMITATION OF ABSTRACT	18. NUMBER OF PAGES	19a. NAME OF RESPONSIBLE PERSON
a. REPORT	b. ABSTRACT	c. THIS PAGE			USAMRMC
U	U	U	UU	30	19b. TELEPHONE NUMBER *(include area code)*

Table of Contents

Introduction

Conventional mammography is limited in its sensitivity for detecting subtle tissue's pathological changes, since the imaging relies on the small differences in x-ray attenuation between the lesions and breast tissues of variable structure. As x-ray traverses a breast, not only does its intensity get attenuated, but its phase also gets shifted. The amount of x-ray phase shift is proportional to x-ray wavelength and the ray integral of breast electron densities. Hence the phase sensitive x-ray imaging has potential for greatly increasing x-ray imaging sensitivity and specificity and reducing radiation doses associated with the imaging.

The approaches for phase-sensitive x-ray imaging fall into three broad categories: the crystal analyzer-based imaging, the phase-gratings based interferometric imaging, and the inline phase-sensitive imaging. Among the three methods the inline phase-sensitive imaging can be implemented without any x-ray optics such as the costly crystal monochromators and crystal analyzers or the hard-to-fabricate expensive diffractive gratings, hence it is especially suitable for clinical imaging implementation. The setting for inline phase-sensitive imaging is very much similar to conventional x-ray imaging, provided spatially coherent x-ray illumination and large subject-detector distance are implemented. The phase-contrast manifests as the interference fringes formed by the phase-shifted x-rays undergoing the Fresnel diffraction.

The long term objective of the project is to develop a low-dose and quantitative phase x-ray imaging technique for facilitating breast cancer detection. The Specific Aims of the project of the three-year period are: (1) Develop prototype phase-imaging system enabling the phase retrieval, that is, the reconstruction of objects phase-maps. The system hardware comprises a micro-focus tube operating at high tube voltages, a high resolution photostimulable phosphor plate (CR-plate) based detector system. The core algorithms for breast phase-map reconstruction will be developed to retrieve a breast phase map from a single recorded image. (2) Validate the accuracy of the reconstructed tissue projected electron densities; validate the many-fold radiation dose reduction achieved with the proposed system; conduct subjective measurements to characterize the performance of the proposed system.

Body

In the second year of this project, as planned in the Statement of Work, we performed two tasks: (A). Continue to develop the robust phase retrieval algorithms for future phase imaging. It is imperative to limit radiation doses involved in any clinical imaging applications. Hence it is important to develop robust phase retrieval approaches against the noise, and thereby to enable radiation dose reduction in phase imaging. In order to develop our new phase retrieval method to its full potential, our efforts in the Year 2 were focused on refining the attenuation-partition based iterative phase retrieval method and performing quantitative and systematic evaluation of its robustness and efficiency compared to the two most widely used phase retrieval algorithms in the literature. (B).Complete the system hardware integration for future phase imaging with breast phantoms.

(A). Refinement and performance evaluation of the attenuation-partition based iterative phase retrieval method

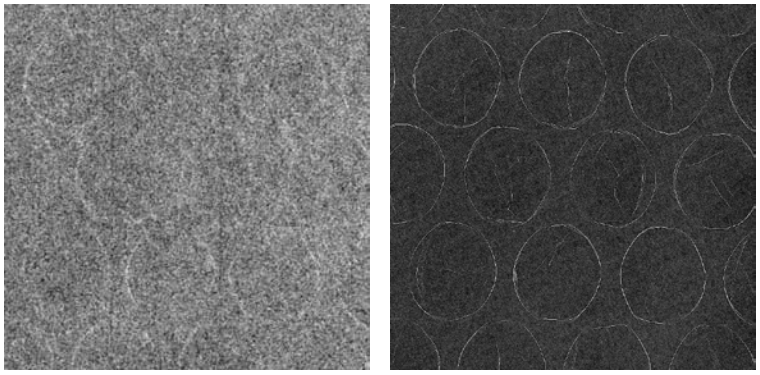

Fig.1. Nylon air bubble Images acquired at 40 kVp, SID = 1.75 m. (left) Conventional radiograph. (right) Phase–contrast image, M = 2.8.

Introduction: When x-ray traverses an object x-ray undergoes phase-shift as well. The differences in x-ray phase shifts between different tissues are about one thousand times greater than the difference in attenuation. A tissue phase map $\varphi(\vec{r})$ is a map of the ray integrals $\varphi(\vec{r}) = -(2\pi/\lambda)\int \delta(\vec{r},s)ds$, where $\delta(\vec{r},s)$ denotes the tissue refractive index decrement. In phase contrast imaging, an important task is to retrieve tissue phase maps. Phase retrieval has potential for improving tissue contrast and achieving quantitative tissue characterization. Moreover, phase retrieval is required for phase sensitive tomography and tomosynthesis for removing artifacts associated x-ray refraction and diffraction.

The mostly used phase retrieval method is based on the Transport Intensity of Equation (TIE). According to the TIE-based method, one acquires two images: one contact radiograph, and one phase contrast image. The phase map $\varphi(\vec{r})$ is retrieved by using the equation $\varphi(\vec{r}) = -(2\pi M/\lambda R_2)\nabla^{-2}\left\{\nabla\cdot\left[\nabla\left(\nabla^{-2}\left(M^2 I/I_{in} - A_o^2\right)\right)\Big/A_o^2\right]\right\}$ [Allen et al. 2001]. The inverse Laplacian operator ∇^{-2} contains a singularity at the zero-frequency in the Fourier domain, we believe that it actually amplifies the noise in images and may fail the phase retrieval. Fig. 1 shows a contact radiograph and a phase contrast image of a nylon air-bubble wrap acquired at 40 kVp from our previous experiment. We then used the two images in Fig. 1 for the phase retrieval. Fig. 2-(left) is the retrieved phase map with the TIE-method [Yan et al. 2008]. Apparently the retrieval failed because of relatively high noise levels in the "low dose" projections. Fig. 2-(middle) is the retrieved phase map with the TIE-method and the Tikhonov regularization [Tikhonov et al. 1977]. The Tikhonov regularization is commonly used regularization method in phase retrievals. It essentially consists of replacing the inverse

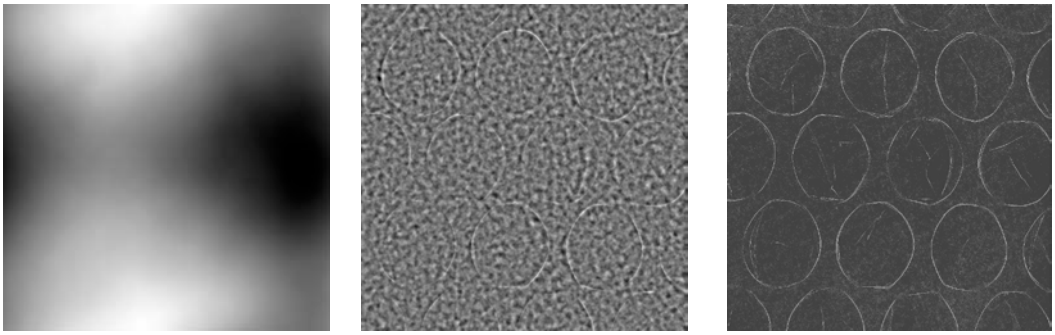

Fig. 2. Retrieved phase maps of the Nylon air bubble wrap from the acquired images in Fig. 1. (left) Erroneous phase map retrieved with the TIE method. (middle) Erroneous phase map retrieved with the TIE method and Tikhonov regularization. (right) Phase map retrieved with the prior knowledge of nylon's attenuation coefficient and refraction index.

Laplacian operator ∇^{-2} by $\nabla^2 \Big/ \left((\nabla^2)^2 + \alpha^2 \right)$, where α is called the Tikhonov regularization parameter. In essence Tikhonov regularization seeks the minimum-norm, least squares solution for phase retrieval. The retrieval result with Tikhonov regularization is still unsatisfactory, as is shown in Fig. (2)-(middle). In contrast, the image shown Fig. 2-(right) is the correctly retrieved phase map using a different method that utilizes the prior knowledge of the single material (nylon) attenuation coefficients and its refraction indices. Unfortunately, the single material-based method does not apply to general inhomogeneous tissues in medical imaging. These findings show that the TIE-based phase-retrieval method suffers from intrinsic instability when the noise presets. The robustness of phase retrieval algorithms against noises in images is critical not only for retrieval accuracies but also for being able to reduce radiation doses involved, since suppressing x-ray quantum noise requires high radiation doses in imaging. In clinical imaging applications it is imperative to limit radiation doses involved, hence it is important to develop robust phase retrieval approach for clinical applications. For general inhomogeneous tissue samples encountered in medical imaging applications, a new phase retrieval method is pressingly needed.

Method: In 2008 we proposed a new phase retrieval method: the attenuation-partition based iterative phase retrieval method [Yan et al. 2008]. We have applied this method to the phase retrievals results for experimental images and found satisfactory results. We have applied this new algorithm to retrieve the phase map of a breast lumpectomy specimen from its contact radiograph and phase contrast image, which were acquired in our previous experiments. We found that the noise spoiled the phase retrieval with the TIE method, and the Tikhonov regularization could not retrieve the phase map of the specimen either. But the attenuation-partition based method, taking only 10 iterations, retrieved the phase map of the specimen [Yan et al. 2008]. However, only qualitative evaluation of the retrieved phase map was made at that time

In order to develop this phase retrieval method to its full potential, in the Year 2 we refined our attenuation-partition based iterative phase retrieval method for speeding up its convergence by modifying the algorithm coding, and performed quantitative and systematic evaluation of its robustness and efficiency compared to the widely used phase retrieval methods in the literature. In order to simulate the morphological features of breast tissues, we first construct a digital breast specimen model. We adopted a radiograph of a breast lumpectomy specimen with pixel values rescaled and the localization wire removed with a pixel-value interpolation. The linear attenuation coefficients and electron densities for the 50% glandular and 50% adipose breast tissues are computed from the tissue's elemental composition and the interpolated elemental mass attenuation coefficients from the standard reference. Moreover, each mass attenuation coefficient is further broken down to two components: one from x-ray photoelectric absorption and coherent scattering, and another from incoherent scattering. In addition, four small ellipsoids of calcium carbonate (CaCO3) are embedded in the specimen model to simulate the breast microcalcification in [Yan et al. 2010]. To simulate the noise encountered in the practice of phase retrieval, we added into the data the Poisson-distribution random noise,

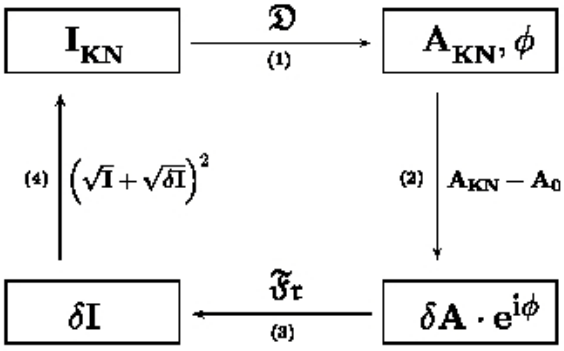

Fig. 3. Flow chart of the attenuation-partition based iterative algorithm for general phase retrieval.

and the error caused by the misalignment between an object's radiograph and its phase-contrast image acquired at a large sample-detector distance. The misalignment could be resulted from the shift or tilting of the object or detector between the two projections. In the algorithm performance analysis, we systematically compared the performance of this new algorithm with two widely used phase retrieval algorithms in the literature, namely the Gerchberg-Saxton (GS) method and the Transport of Intensity Equation (TIE) method [Allen et al. 2001].

The flow chart of our attenuation-partition based iterative algorithm is shown in Fig. 3. In this flow chart A_o^2 denotes the attenuation-contrast image, and A_{KN}^2 the Compton-scattering contrast image, ϕ the phase map, I the phase contrast projection image, and the hypothetical phase contrast image formed by the sample electron densities only. Two transforms are implemented in Fig. 3, one is the Fresnel diffraction transform, the other is the phase-attenuation duality transform [Yan et al. 2010]. Our idea underlining the algorithm flow chart is: use the correlation of tissue attenuation cross-section with its phase cross-section to eliminate the singularity in the phase retrieval operator. This is an extension to general samples of the phase-attenuation duality for soft tissues [Wu et al. 2005]. we first isolates the Compton scattering cross-sections from tissue's total attenuation image, and correlate the Compton scattering cross-section with tissue's phase cross-section, and retrieve an approximate phase map by the phase-attenuation duality method [Wu et al. 2005], which is singularity-free and intrinsically stable. We then iteratively incorporate the rest attenuation cross-section into phase

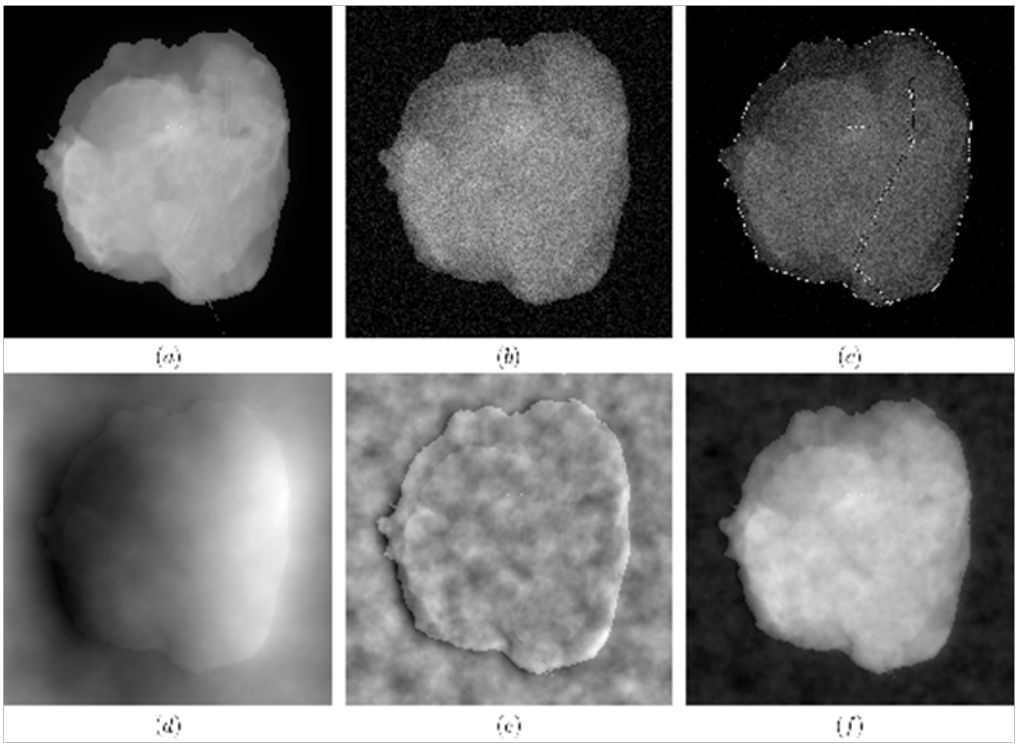

Fig. 4. Comparison of the TIE method and the AP-based method with the noise added in the simulations. (a) The true phase map. (b) Contact radiograph with noise. (c) Normalized phase contrast image with noise. (d) Phase map recovered with the TIE algorithm but without Tikhonov regularization. (e) Phase map recovered with TIE algorithm and with Tikhonov regularization; (f) Phase map recovered with the APBA after 10 iteration steps. Note that the enhanced track in (c) is formed from the phase-sensitive projection of small residual variations along the removed guide-wire track in the digital specimen model.

retrieval by repeatedly correcting errors, which is calculated as the differences between the measured image intensities and the Fresnel diffraction estimates [Yan et al. 2010].

Result: In the second period of this project we refined our attenuation-partition based iterative phase retrieval method for speeding up its convergence. We systematically and quantitatively compared the performance of this algorithm with other two widely used phase retrieval algorithms, namely the Gerchberg-Saxton (GS) method and the Transport of Intensity Equation (TIE) based method. The systematic comparison is conducted by analyzing phase retrieval performances with a digital breast lumpectomy specimen model. We show that the proposed algorithm converges faster than the GS algorithm in the Fresnel diffraction regime, and is much more robust against image noise than the TIE algorithm. As an example, Fig. 4 (a)-(f) show the comparison of the TIE method and our attenuation-partition based method for the digital breast lumpectomy specimen model. Our work was published in *Optics Express* in July 2010 [Yan et al. 2010]. The paper is enclosed in the Appendix of this report for review.

(B). Build the prototype system

Since the project does not support equipment purchase, most of the system components are those available from our subcontractor Dr. Liu's laboratory at University of Oklahoma. Dr. Liu and his group performed the works of integrating the hardware components to a prototype system. The system hardware integration have been continued in this period. In last period, during the hardware integration, the tube assembly malfunction occurred, and eventually the tube assembly and its controller failed. After tedious efforts in dealing with the OU offices and the vendor (Hamamatsu Photonics) for the repair costs and repair arrangements, finally a working source system becomes available in this period. The system integration is completed in this period. The completed High Energy X-Ray Phase Contrast Imaging System, as is shown in Fig. 5, is briefly described as follows.

Fig. 5. A high energy x-ray phase contrast imaging system

The X-ray Source (the red box in Fig. 5): The source is a microfocus x-ray source (Model L8121-03, Hamamatsu Photonics, Japan) was utilized for the system. The x-ray tube consists of a tungsten target and a Beryllium output window. The tube has a tungsten-target and a uniform circular focal spot of 50 μm in diameter for 75 W power loading, and a focal spot of 7 μm for tube 10 W, and the tube can operate at up to 150 kVp.

The Image Detector (Fig. 5): Since tissue phase-contrast fringes recorded is proportional to the Laplacian and gradient of phase-shifts, hence the detector should have high sampling frequency. The image detection system was a computed radiography system with mammography plates (Regius 190, Konica Minolta Medical Imaging, Wayne, New Jersey) with dimensions of 24 by 30 centimeters (cm). The mammography plates were designed with a focus on optimizing the image formulation based on low energies, which may not provide optimal results at high energies. The use of general radiography plates may be beneficial instead, due to the alternate design for utilization at high energies. However, the CR system processes the mammography plates with a pixel pitch of $43.75\,\mu m$, while general radiography plates are processed with a pixel pitch of $87.5\,\mu m$. Due to the fact that the mammography images are produced with double the spatial resolution, they were used for acquisition of the initial images. However, the next step in this research is to investigate the tradeoff between the higher spatial resolution of the mammography plate with the higher quantum efficiency of the general radiography plate, to determine which of the plates provides optimal images at high energies.

The Geometric Configuration Setting on an Optical Bench (Fig. 5): In order to operate the prototype in both conventional and phase contrast imaging modes for comparisons, the imaging and measurement components (the x-ray tube, CR-plate) are mounted on an optical rail, which allows to vary the source-object distance $\mathbf{R_1}$ and object-detector distance $\mathbf{R_2}$ as needed. It allows a SID of 1.83 m. The object to detector distance $\mathbf{R_2}$ should be sufficiently large as well to allow phase-shifted x-rays to diffract as forming a phase-contrast image. This is because the imaging-geometry should optimize the phase contrast visibility by balancing the conflict

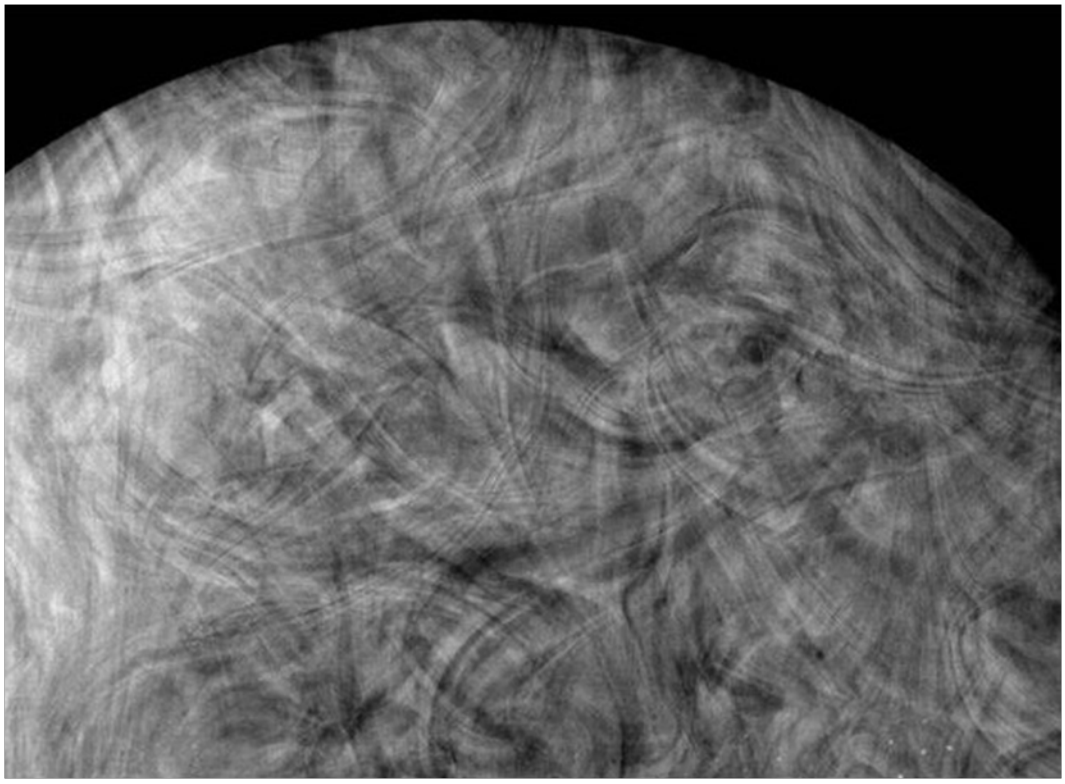

Fig. 6. Image of the Mammography BR3D phantom (140 kVp, 6.4 mAs.)

requirements of x-ray spatial coherence, large diffraction fringes and finite sizes of the focal spot size and finite detector pitch. In a previous work we found that the phase-contrast that could be imaged is proportional to the relative phase-visibility factor (RPF) [Wu et al. 2004]. From the estimated relative phase-visibility factors with different geometric setting for this system, the optimal magnification factors are found to be in the range of 2 to 2.3.

Preliminary Testing**:** Phantoms were used for demonstrating the system's functionality with high energy x-rays. One of the test images is shown in Fig. 6. This is an Image of the Mammography BR3D phantom (Model 020, CIRS, Norfolk, Virginia), which provides tissue equivalent images for qualitative assessment of image quality. The phantom simulates a realistic clinical image, not only through its composition, which is 100% adipose and glandular tissues blended together in an approximate 50/50 ratio, but also through the 5 cm thickness. In addition, the fifth 10 mm layer of the phantom is a target slab imbedded with targets such as specks, masses and fibers. The image as acquired with a high energy phase contrast prototype system using a Hamamatsu x-ray source with a focal spot size of 7 μm and a Konica-Minolta Computed Radiography System with mammography plates. The SID was 1.83 m, and the SOD was 0.91m feet, which deliver a magnification factor of 2 for the phase contrast images. The image was acquired at an experimental setting of 140 kV, 6.3 mAs (71 μA, 90s.)

In summary, the system hardware integration has been completed in this period. The tests showed that the system is functional for phase contrast image acquisition with high energy x-rays. The efforts for technique optimization are under the way. Especially, we will continue to seek the ways to match the CR-plate's quantum detection efficiencies with the high energy x-rays as the tube operating at 120-150 kVp. One way is to use the general radiography CR-plates of a pixel pitch of $87.5\,\mu m$, and investigate the tradeoff between the higher spatial resolution of the mammography plate with the higher quantum efficiency of the general radiography plate, to determine which of the plates provides optimal phase contrast images at high energies. Another possible better solution is to keep reading the general radiology CR-plates in the high sampling mode of the Konica REGIUS 190 Reader. But so far the vendor is resisting to give us the access code for the reader control for using this unusual sampling method.

Key Research Accomplishments

- It is imperative to limit radiation doses involved in any clinical imaging applications. Hence it is important to develop robust phase retrieval approaches against the noise, and thereby to enable radiation dose reduction in phase imaging. The mostly used phase retrieval method is based on the Transport Intensity of Equation (TIE). We showed that the TIE method fails to provide robust phase retrievals against image noise and the alignment errors. In this period we refined the attenuation-partition based phase retrieval method for speeding up the iteration convergence, and systematically and quantitatively compared its performance against that of the TIE-based method. A digital breast lumpectomy specimen model was constructed for facilitating the quantitative evaluations. We showed that the attenuation-partition based phase retrieval method converges faster than the GS method, and is much more robust against image noise and the alignment errors than the TIE-based method does.

- The system hardware integration has been completed in this period. The tests showed that the system is functional for phase contrast image acquisition with high energy x-rays. The efforts for technique optimization are under the way.

Reportable Outcomes

In this project period we have published the research results in peer-reviewed journals and presented the work in an international conference, as listed in the following.

Peer-Reviewed Journal Article**:**

A. Yan, X. Wu, H. Liu, Performance analysis of the attenuation-partition based iterative phase retrieval algorithm for in-line phase-contrast imaging, Optics Express 18: 16074-16089 (2010)

This journal is the top-ranking journal in terms of the Impact Factor among all sixty-four journals in the field of Optics.

Published Abstract and Conference Presentation**:**

X. Wu**,** A. Yan, H. Liu, Improving robustness of phase retrieval in x-ray phase contrast imaging, Medical Physics 37: 3357 (2010)

X. Wu, A. Yan , H. Liu, "Improving robustness of phase retrieval in x-ray phase contrast imaging," Oral Presentation at the 52nd Annual Meeting of the American Association of Physicists in Medicine, July 19, 2010, Philadelphia, PA.

Conclusion

With the support by USAMRMC we have successfully conducted studies on x-ray phase imaging in the second period of this project. In this period, we focused on the development of a new phase retrieval method that is robust against the noise, and thereby enabling radiation dose reduction in phase imaging. We showed that the mostly used phase retrieval method (the TIE method) fails to provide robust phase retrievals against image noise and the alignment errors. In this period we refined the attenuation-partition based phase retrieval method for speeding up the iteration convergence, and systematically and quantitatively compared its performance against that of the widely used method. A digital breast lumpectomy specimen model was constructed for facilitating the quantitative evaluations. We showed that the proposed method is much more robust against image noise and the alignment errors than the mostly used method does. This new method enables large radiation dose saving in phase-sensitive imaging

In this period we have completed the system hardware integration. The tests demonstrated that the system is functioning for phase contrast image acquisition with high energy x-rays. The efforts for technique optimization are under the way.

In the coming third period we will continue the efforts in improving the prototype's performance. Especially, we will continue to seek the ways to match the CR-plate's quantum detection efficiencies with the high energy x-rays from the tube operating at 120-150 kVp. With the planned use of general radiography CR-plates of a pixel pitch of $87.5\,\mu m$, we will especially need to incorporate the detector response into the phase retrieval algorithms for accurate phase retrieval. We will conduct phase imaging experiments with custom-made breast phantoms, and will reconstruct the phase maps of the phantoms. We will experimentally verify the radiation dose saving with the phase imaging with high energy x-rays, and verify the accuracies of the reconstructed maps of the projected electron densities of the imaged phantoms.

References:

Allen L, Oxley M. 2001. Phase retrieval from series of images obtained by defocus variation, Optics Communications 199: 65-75.

Wu X, Liu H. 2004. A new theory of phase-contrast x-ray imaging based on Wigner distributions. *Medical Physics* 31, 2378-2384.

Wu X, Liu, H, Yan, A. 2005. X-ray phase-attenuation duality and phase retrieval, Optics Letters 30: 379-381.

Tikhonov A , Arsenin V. 1977, *Solution of Ill-posed Problems* (Winston & Sons, Washington.)

Yan A, Wu X, Liu H. 2008. An attenuation-partition based iterative phase retrieval algorithm for in-line phase-contrast imaging, Optics Express 16: 13330-13341.

Yan A, Wu X, Liu H. 2010. Performance analysis of the attenuation-partition based iterative phase retrieval algorithm for in-line phase-contrast imaging, Optics Express 18: 16074-16089.

Appendices

Copies of following publications are enclosed for review.

Peer-Reviewed Journal Article**:**

A. Yan, X. Wu, H. Liu, Performance analysis of the attenuation-partition based iterative phase retrieval algorithm for in-line phase-contrast imaging, Optics Express 18: 16074-16089 (2010)

Published Abstract**:**

X. Wu**,** A. Yan, H. Liu, Improving robustness of phase retrieval in x-ray phase contrast imaging, Medical Physics 37: 3357 (2010)

Performance analysis of the attenuation-partition based iterative phase retrieval algorithm for in-line phase-contrast imaging

Aimin Yan,[1,*] **Xizeng Wu,**[1,*] **and Hong Liu** [2]

[1] *Department of Radiology, University of Alabama at Birmingham, Birmingham, AL 35233, USA*

[2] *Center for Bioengineering and School of Electrical and Computer Engineering, University of Oklahoma, Norman, OK 73019, USA*

[*] *Corresponding authors: ayan@uabmc.edu, xwu@uabmc.edu*

Abstract: The phase retrieval is an important task in x-ray phase contrast imaging. The robustness of phase retrieval is especially important for potential medical imaging applications such as phase contrast mammography. Recently the authors developed an iterative phase retrieval algorithm, the attenuation-partition based algorithm, for the phase retrieval in inline phase-contrast imaging [1]. Applied to experimental images, the algorithm was proven to be fast and robust. However, a quantitative analysis of the performance of this new algorithm is desirable. In this work, we systematically compared the performance of this algorithm with other two widely used phase retrieval algorithms, namely the Gerchberg-Saxton (GS) algorithm and the Transport of Intensity Equation (TIE) algorithm. The systematical comparison is conducted by analyzing phase retrieval performances with a digital breast specimen model. We show that the proposed algorithm converges faster than the GS algorithm in the Fresnel diffraction regime, and is more robust against image noise than the TIE algorithm. These results suggest the significance of the proposed algorithm for future medical applications with the x-ray phase contrast imaging technique.

OCIS codes: 340.7440 (X-ray imaging); 030.1670 (Coherent optical effects)

References and links

1. A. Yan, X. Wu, and H. Liu, "An attenuation-partition based iterative phase retrieval algorithm for in-line phase-contrast imaging," Opt. Express **16**, 13,330 – 13,341 (2008).
2. S. Wilkins, T. Gureyev, D. Gao, A. Pogany, and A. Stevenson, "Phase-contrast imaging using polychromatic hard X-rays," Nature **384**, 335 – 338 (1996).
3. A. Snigirev, I. Snigireva, V. Kohn, S. Kuznetsov, and I. Shelokov, "On the possibilities of x-ray phase contrast microimaging by coherent high-energy synchrotron radiation," Rev. Sci. Instrum. **66**, 5486 – 5492 (1995).
4. K. Nugent, T. Gureyev, D. Cookson, D. Paganin, and Z. Barnea, "Quantitative Phase Imaging Using Hard X Rays," Phy. Rev. Lett. **77**, 2961 – 2965 (1996).
5. A. Pogany, D. Gao, and S. Wilkins, "Contrast and resolution in imaging with a microfocus x-ray source," Rev. Sci. Instrum. **68**, 2774 – 2782 (1997).
6. F. Arfelli, V. Bonvicini, and et al, "Mammography with synchrotron radiation: phase-detected Techniques," Radiology **215**, 286 – 293 (2000).

#126430 - $15.00 USD Received 2 Apr 2010; revised 11 Jun 2010; accepted 9 Jul 2010; published 15 Jul 2010

7. D. Paganin, S. Mayo, T. Gureyev, P. Miller, and S. Wilkins, "Simultaneous phase and amplitude extraction from a single defocused image of a homogeneous object," J. Microsc. **206**, 33 – 40 (2002).
8. S. Mayo, T. Davis, T. Gureyev, P. Miller, D. Poganin, A. Pogany, A. Stevenson, and S. Wilkins, "X-ray phase-contrast microscopy and microtomography," Opt. Express **11**, 2289 – 2302 (2003).
9. X. Wu and H. Liu, "A general theoretical formalism for X-ray phase contrast imaging," J. X-ray Sci. and Tech. **11**, 33 – 42 (2003).
10. X. Wu and H. Liu, "Clinical implementation of phase-contrast x-ray imaging: Theoretical foundations and design considerations," Med. Phys. **30**, 2169 – 2179 (2003).
11. X. Wu and H. Liu, "A new theory of phase-contrast x-ray imaging based on Wigner distributions," Med. Phys. **31**, 2378 – 2384 (2004).
12. E. Donnelly, R. Price, and D. Pickens, "Experimental validation of the Wigner distributions theory of phase-contrast imaging," Med. Phys. **32**, 928 – 931 (2005).
13. D. Zhang, M. Donvan, L. Fajardo, A. Archer, X. Wu, and H. Liu, "Preliminary feasibility study of an in-line phase contrast x-ray imaging prototype," IEEE Trans. Biomed. Eng. **55**, 2249 – 2257 (2008).
14. X. Wu, H. Liu, and A. Yan, "X-ray phase-attenuation duality and phase retrieval," Opt. Lett. **30**(4), 379 – 381 (2005).
15. X. Wu and H. Liu, "X-Ray cone-beam phase tomography formulas based on phase-attenuation duality," Opt. Express **13**, 6000 – 6014 (2005).
16. P. Cloetens, R. Mache, M. Schlenker, and S. Lerbs-Mache, "Quantitative phase tomography of Arabidopsis seeds reveals intercellular void network," PNAS **103**, 14,626 – 14,630 (2006).
17. X. Wu, H. Liu, and A. Yan, "Phase-Contrast X-Ray Tomography: Contrast Mechanism and Roles of Phase Retrieval," Eur. J. Radiology **68**, S8 – S12 (2008).
18. D. Paganin and K. Nugent, "Noninterferometric Phase Imaging with Partially Coherent Light," Phy. Rev. Lett. **80**, 2586 – 2589 (1998).
19. X. Wu and H. Liu, "A dual detector approach for X-ray attenuation and phase imaging," J. X-ray Sci. and Tech. **12**, 35–42 (2004).
20. X. Wu and H. Liu, "Phase-space evolution of x-ray coherence in phase-sensitive imaging," Appl. Opt. **47**, E44 – E52 (2008).
21. M. Teague, "Deterministic phase retrieval: a Green's function solution," J. Opt. Soc. Am. **73**, 1434 – 1441 (1983).
22. T. Gureyev, Y. Nesterets, D. Paganin, A. Pogany, and S. Wilkins, "Linear algorithms for phase retrieval in the Fresnel region. 2. Partially coherent illumination," Opt. Comm. **259**, 569 – 580 (2006).
23. J. Guigay, M. Langer, R. Boistel, and P. Cloetens, "Mixed transfer function and transport of intensity approach for phase retrieval in the Fresnel region," Opt. Lett. **32**, 1617 – 1619 (2007).
24. X. Wu and A. Yan, "Phase Retrieval From One Single Phase Contrast X-Ray Image," Opt. Express p. Opt. Express **17**, 11187 – 11196 (2009).
25. L. Allen and M. Oxley, "Phase retrieval from series of images obtained by defocus variation," Opt. Comm. **199**, 65 – 75 (2001).
26. R. W. Gerchberg and W. O. Saxton, "A practical algorithm for the determination of the phase from image and diffraction plane pictures," Optik **35**, 237 – 246 (1972).
27. J. Fienup, "Reconstruction of an object from the modulus of its Fourier Transform," Opt. Lett. **3**, 27 – 29 (1978).
28. J. Fienup, "Phase retrieval algorithms: a comparison," Appl. Opt. **21**, 2758 – 2769 (1982).
29. N. Dyson, *X-Rays in Atomic and Nuclear Physics* (Longman Scientific and Technical, Essex, UK, 1973).
30. X. Wu, A. Dean, and H. Liu, *Biomedical Photonics Handbook*, chap. 26, pp. 26-1 – 26-34 (CRC Press, Tampa, Fla., 2003).
31. J. H. Hubbell, W. I. Veigele, E. A. Briggs, et al., "Atomic form factors, incohoerent scattering functions, and photon scattering cross sections," Journal of Physical Chemistry Reference Data **4**, 471–538 (1975);
32. L. Rudin, "Images, numerical analysis of singularities and shock filters," Report #TR:5250:87, Caltech, C,S, Dept. (1987).
33. L. I. Rudin, S. Osher, and E. Fatemi, "Nonlinear total variation based noise removal algorithms," Physica D **60**, 259 – 268 (1992).
34. X. Wu, G.T. Barnes and D.M. Tucker, "Spectral dependence of glandular tissue dose in screen-film mammography," Radiology **179**, 143 – 148 (1991).
35. X. Wu, E.L. Gingold, G.T. Barnes and D.M. Tucker, "Normalized average glandular dose in Molybdenum target-Rhodium filter and Rhodium target-Rhodium filter mammography," Radiology **193**, 83 – 89 (1994).
36. J. Seldin and J. Fienup, "Numerical investigation of the uniqueness of phase retrieval," J. Opt. Soc. Am. A **7**(3), 412 – 427 (1990).
37. F. Roddier and C. Roddier, "Wavefront reconstruction using Iterative Fourier transforms," Appl. Opt. **30**, 1325 – 1327 (1991).
38. C. Roddier and F. Roddier, "Wave-front reconstruction from defocused images and the testing of ground-based optical telescopes," J. Opt. Soc. Am. A **10**, 2277 – 2287 (1993).
39. T. Gureyev, A. Roberts, and K. Nugent, "Partially coherent fields, the transport-of-intensity equation, and phase uniqueness," J. Opt. Soc. Am. A **12**, 1942 – 1946 (1995).

#126430 - $15.00 USD Received 2 Apr 2010; revised 11 Jun 2010; accepted 9 Jul 2010; published 15 Jul 2010

40. T. Gureyev and K. Nugent, "Phase retrieval with the transport-of-intensity equation. II. Orthogonal series solution for nonuniform illumination," J. Opt. Soc. Am. A **13**, 1670 – 1682 (1996).
41. A. Tychonoff and V. Arsenin, *Solution of Ill-posed Problems* (Winston & Sons, Washington, 1977).

1. Introduction

Differing from the conventional x-ray imaging, which relies on the small differences in x-ray attenuation changes between tissues variable structure, inline phase contrast imaging is based on the tissues' phase-shifts diffraction from the object to the detector. Since x-ray phase-shift differences between tissue and lesions are about one thousand times larger than attenuation differences [2, 3, 4], x-ray phase contrast imaging has the potential to enhance the lesion detection sensitivity and specificity, and reduce the radiation dose compared to conventional x-ray imaging. In the inline phase contrast imaging, the diffracted phase-shifts form bright and dark fringes at tissue boundaries and this bright and dark fringes are called edge enhancement. The edge enhancement relies on the spatial coherence of the x-ray source, the Laplacian and gradients of x-ray phase-shifts caused by the tissue, and the gradients of the objects attenuation [5, 6, 7, 8, 9, 10, 11, 12, 13, 14, 15]. One procedure of phase contrast imaging is to disentangle tissue phase-shifts from the mixed contrast mechanism and recover the phase maps from acquired phase contrast images. This procedure is called phase retrieval. Phase retrieval technique plays a central role in phase contrast x-ray imaging. By means of phase retrieval, one can reconstruct a quantitative map of phase-shifts, a phase image of the imaged object [4, 7, 14, 16, 17]. The amount of x-ray phase-shifts ϕ by tissues is determined by

$$\phi(\vec{\mathbf{r}}) = -\left(\frac{hc}{E}\right) r_{\mathrm{e}} \int \rho_e(\vec{\mathbf{r}}, z) dz = -\left(\frac{hc}{E}\right) r_{\mathrm{e}} \rho_{\mathrm{e,p}}(\vec{\mathbf{r}}), \tag{1}$$

where r_{e} is the classical electron radius, h the Plank constant, c the speed of light, E the x-ray photon energy, and $\rho_{\mathrm{e,p}}$, the integration of the electron density ρ_e over the x-ray path, is called the projected electron density [2, 3, 4]. So a retrieved phase map is equivalently a map of imaged object's quantitative projected electron densities. Moreover, phase retrieval is also a necessary procedure for phase-sensitive volumetric imaging, such as the phase sensitive tomography and tomosynthesis, to acquire the artifact free 3D images of object attenuation coefficients and electron densities [8, 15, 16].

Phase retrieval is based on x-ray propagation equation derived either from the Fresnel diffraction or the Wigner distribution based phase-space formalism [5, 18, 9, 19, 20]. To be specific, let $\phi(\vec{\mathbf{r}})$ be the x-ray phase-shift caused by the imaged object, and $A_0(\vec{\mathbf{r}})$ the x-ray transmission, or the attenuation-map of the object. Then the Fourier transform of the x-ray intensity, $\hat{\mathscr{F}}(I)(\vec{u}) = \int_{\mathbb{R}^2} I(\vec{x}) \exp[2\pi i \vec{x} \cdot \vec{u}]\, d\vec{x}$, at position away from the object with distance R_2, of the monochromatic point x-ray source starting at a place away from the object R_1 distance, can be modeled by the following [9]

$$\begin{aligned}
\hat{\mathscr{F}}(I)\left(\frac{\vec{\mathbf{u}}}{M}; R_1 + R_2\right) = I_{\mathrm{in}} \Bigg\{ & \cos\left(\frac{\pi\lambda R_2}{M}\vec{\mathbf{u}}^2\right) \cdot \hat{\mathscr{F}}\left(A_0^2\right) + \\
& + \left[2\sin\left(\frac{\pi\lambda R_2}{M}\vec{\mathbf{u}}^2\right) - \left(\frac{2\pi\lambda R_2}{M}\vec{\mathbf{u}}^2\right) \cdot \cos\left(\frac{\pi\lambda R_2}{M}\vec{\mathbf{u}}^2\right)\right] \cdot \hat{\mathscr{F}}\left(A_0^2\phi\right) - \\
& - \cos\left(\frac{\pi\lambda R_2}{M}\vec{\mathbf{u}}^2\right) \cdot \frac{\lambda R_2}{2\pi M} \cdot \hat{\mathscr{F}}\left(\nabla \cdot \left(A_0^2 \nabla\phi\right)\right) - \\
& - \frac{\lambda R_2}{4\pi M} \sin\left(\frac{\pi\lambda R_2}{M}\vec{\mathbf{u}}^2\right) \cdot \hat{\mathscr{F}}\left(\nabla^2 A_0^2\right) \Bigg\},
\end{aligned} \tag{2}$$

#126430 - $15.00 USD Received 2 Apr 2010; revised 11 Jun 2010; accepted 9 Jul 2010; published 15 Jul 2010

where I_{in} is the incident x-ray intensity at R_1, λ the wavelength of the monochromatic point x-ray source and $M = (R_1 + R_2)/R_1$ is the geometric magnification. When the FT-Space Fresnel propagator $\pi\lambda R_2\vec{u}^2/M \ll 1$, Eq. (2) can be simplified to the Transport of Intensity Equation (TIE) [21, 4, 9]

$$I(\vec{\mathbf{r}}; R_1 + R_2) = \frac{I_{\text{in}}}{M^2}\left\{A_0^2\left(\frac{\vec{\mathbf{r}}}{M}\right) - \frac{\lambda R_2}{2\pi M}\nabla\cdot\left(A_0^2\nabla\phi\right)\left(\frac{\vec{\mathbf{r}}}{M}\right)\right\}. \tag{3}$$

It is worthy to note that Eq. (3) is valid only for moderate resolution images. For high resolution images, i.e. when the FT-Space Fresnel propagator $\pi\lambda R_2\vec{u}^2/M$ is close or greater than π, any phase retrieval algorithms based on Eq. (3) need to be substituted to Eq. (2) [22, 23, 24]. In this paper, the algorithms discussed are all based on Eq. (3), i.e. the moderate resolution is satisfied.

Numerous algorithms have been suggested on how to effectively recover the phase-shift from the phase contrast images. Among these, two algorithms are most widely used. One is the TIE algorithm implemented by Allen and Oxley in [25]. The other is the GS algorithm developed first by Gerchberg and Saxton in [26] and later improved by Fienup [27, 28]. These two algorithms have both their advantages and disadvantages. The TIE algorithm is a direct approximate method which is fast but is unstable with noisy data; the GS algorithm on the other hand is relatively more stable than the TIE algorithm[25] but the converging speed is slow especially for the field of medical imaging. In [1], the authors developed an Attenuation-Partition Based Algorithm (APBA) based on the phase-attenuation duality property of soft tissues under higher x-ray energy. This algorithm is fast and stable for potential medical imaging. We compared the performance of this algorithm with the TIE algorithm for two groups of data under the condition of medical imaging in [1], including the phase retrieval from phase-contrast images of a breast lumpectomy specimen. In this paper, we will make a systematic analysis about this algorithm and compare its performance with the one of the GS algorithm and the TIE algorithm with simulated data.

The paper is organized as follows. In Section 2, we first summarize the attenuation-partition based algorithm (APBA), which is motivated by our observation of the phase-attenuation duality[14]. Then we give a measure, called total variation, used to evaluate the closeness of two image data. This measure is used as a quantitative standard in comparing the performance between different algorithms in the following section. In Section 3, we first develop a breast specimen model which can reflect the attenuation and phase changes with respect to the x-ray energy change (Section3.1), and then compare the performance of the algorithm with the GS algorithm (Section 3.2) and the TIE algorithm (Section 3.3). Finally, we conclude this paper in Section 4.

2. The attenuation-partition based algorithm (APBA) and an image accuracy measure

2.1. The Attenuation-Partition Based Algorithm

The attenuation-partition based algorithm (APBA) is a recently developed iterative algorithm for phase retrieval[1]. It was derived from our previous notion of the phase-attenuation duality[14], and it takes advantage of the correlation between the attenuation and phase-shift for phase retrieval. As is well known, tissue's attenuation change A_0 in the diagnostic x-ray imaging arose from three x-ray and tissue interactions: the photoelectric absorption, the coherent scattering, and the incoherent scattering[29, 30, 9, 14]. However, among the three interactions, the attenuation caused by incoherent scattering A_{KN}, which is dominated by the x-ray Compton scattering, deserves a special attention. This is because both of A_{KN} and the x-ray phase-shift ϕ are determined by the tissue's projected electron density:

$$A_{\text{KN}}(\vec{\mathbf{r}}) = \exp\left[-\frac{\sigma_{\text{KN}}}{2}\rho_{\text{e,p}}(\vec{\mathbf{r}})\right], \qquad \phi(\vec{\mathbf{r}}) = -\lambda r_{\text{e}}\rho_{\text{e,p}}, \tag{4}$$

#126430 - $15.00 USD Received 2 Apr 2010; revised 11 Jun 2010; accepted 9 Jul 2010; published 15 Jul 2010

where λ is the x-ray wavelength, r_e the classical electron radius, $\rho_{e,p}$ the projected electron density as defined in Eq. (1), and σ_{KN} is the total cross section for x-ray Compton scattering with a free electron:

$$\sigma_{KN}(E_{photon}) = 2\pi r_e^2 \left\{ \frac{1+\eta}{\eta^2} \left[\frac{2(1+\eta)}{1+2\eta} - \frac{1}{\eta}\log(1+2\eta) \right] + \right. \\ \left. + \frac{1}{2\eta}\log(1+2\eta) - \frac{1+3\eta}{(1+2\eta)^2} \right\}, \quad (5)$$

with $\eta = E_{photon}/m_e c^2$. Here we denote the photon energy of the primary x-ray beam by E_{photon} and $m_e c^2$ is the rest electron energy. Eq.(4) suggests clearly that the x-ray attenuation and phase-shift by tissue has certain correlation. Our idea is to utilize this correlation for facilitating the phase retrieval.

Of course, the extent of this correlation between phase and attenuation depends on the x-rays photon energy as well as the tissues physical composition. For example, for light elements with atomic numbers $Z \leq 10$, x-ray attenuation is dominated by the Compton scattering for x-rays of 60 keV or higher, i.e. $A_0 \approx A_{KN}$[14]. We call this relationship between phase-shift and attenuation the phase-attenuation duality. The phase-attenuation duality can be used for phase retrieval as follows. Consider a phase contrast imaging setting with a point source of wavelength λ. The object is at a distance R_1 from the source. We denote R_2 as the distance from object to detector plane, $M = (R_1 + R_2)/R_1$ the geometric magnification factor, I_{in} the entrance x-ray intensity at R_1, and $I_D(\vec{r}_D)$ the x-ray intensity at the detector plane. For convenience, we denote $I = M^2 \cdot I_D(\vec{r}_D)/I_{in}$ as the normalized intensity of phase-contrast image. When the phase-attenuation duality holds, the phase map $\phi(\vec{r})$ can be robustly retrieved from just a single projection image[14]:

$$A_{KN}^2(\vec{\mathbf{r}}) = \mathfrak{D}(I) = \hat{\mathscr{F}}^{-1}\left(\frac{\hat{\mathscr{F}}(I)}{1+4\pi^2\tilde{k}\vec{\mathbf{u}}^2} \right), \qquad \phi(\vec{r}) = \left(\frac{\lambda r_e}{\sigma_{KN}} \right) \ln\left(A_{KN}^2(\vec{r}) \right), \quad (6)$$

where

$$\tilde{k} = \frac{\lambda R_2}{2\pi M} \cdot \frac{\lambda r_e}{\sigma_{KN}}, \quad (7)$$

and $\mathfrak{D}$, for sake of convenience, is called the "duality transform" acting on the normalized image I.

In general imaging cases, such as with low energy x-rays or an object contains calcified tissues such as calcification, this phase-attenuation duality does not hold. However, we can still factor out tissue's total attenuation A_0 as

$$A_0(\vec{\mathbf{r}}) = A_{KN}(\vec{\mathbf{r}}) \cdot A_{pe,coh}(\vec{\mathbf{r}}), \quad (8)$$

where we denote the attenuation caused by photoelectric absorption and coherent scattering by $A_{pe,coh}$. Strictly speaking, σ_{KN} is only Compton scattering cross-section, it may be slightly different from the incoherent scattering cross-section for high-Z elements. This is because while Compton scattering is x-ray scattering from the free electrons, the incoherent scattering is that from the bound atomic electrons[31]. So when we factor $A_0 = A_{KN} \cdot A_{pe,coh}$ (Eq. (8)) we actually factor the small residual binding effect of atomic electrons into $A_{pe,coh}$. With this understanding, Eqs.(4) and (8) are rigorously valid. The notion of Eq. (6) and Eq. (8) led us to the development of the attenuation-partition based algorithm [1]. While the derivations and the algorithm details of this method can be found from Ref. [1], a brief description of the method is as follows. Our goal is to retrieve the phase map from the two normalized images: one is the object's

#126430 - $15.00 USD Received 2 Apr 2010; revised 11 Jun 2010; accepted 9 Jul 2010; published 15 Jul 2010

attenuation image A_0^2 acquired with $R_2 = 0$, and the other is the acquired phase contrast image $I = M^2 \cdot I_D(\vec{r}_D)/I_{\text{in}}$ with $R_2 > 0$. Employing the acquired phase contrast image I and the duality transform Eq. (6), we will first obtain an estimate for the attenuation-component A_{KN} and phase map ϕ. We then rewrite Eq. (8) as

$$A_0 = A_{\text{KN}} - \delta A, \qquad \delta A = A_{\text{KN}}(1 - A_{\text{pe,coh}}), \tag{9}$$

and find the correction term δA using the estimate of A_{KN}. We then employing the Fresnel Diffraction transform (as defined in Eq. (11)) to transport the wavefield $\delta A e^{i\phi}$ from R_1 to R_2. We can find $\delta I = \left|\mathfrak{F}_{\mathfrak{r}}\left(\delta A e^{i\phi}\right)\right|^2$, which is the difference between phase contrast image I and the "duality-only" counterpart $I_{\text{KN}} = \left|\mathfrak{F}_{\mathfrak{r}}\left(A_{\text{KN}} e^{i\phi}\right)\right|^2$. With the corrected "duality-only" image intensity $I_{\text{KN}} = \left(\sqrt{I} + \sqrt{\delta I}\right)^2$ we can start a new round of iterations by repeating above procedure. For a rigorous analysis of the iterative algorithm and its convergence interesting readers are referred to [1]. Note that the equation $\sqrt{I} = \sqrt{I_{KN}} - \sqrt{\delta I}$ is generally valid, since it is actually a result of x-ray Fresnel diffraction and extremely smallness of hard x-ray wavelength compared to finest resolution achievable in the phase contrast imaging. While interesting readers can find the mathematical proof of this equation in [1], an intuitive explanation of this formula comes from the x-ray propagation. In such a wave propagation process, or the so-called semiclassical wave propagation, the phase of a wave field evolves essentially according to the free-space Hamilton-Jacobi equation from its initial phase value. So if we denote the Fresnel free propagation as a Fresnel transform $\mathfrak{F}_{\mathfrak{r}}$ acting on the initial wavefield, therefore the two resulted wavefields $\mathfrak{F}_{\mathfrak{r}}(A_{\text{KN}} \exp[i\phi])$ and $\mathfrak{F}_{\mathfrak{r}}(\delta A \exp[i\phi])$ would have the same resultant phases, so the resultant amplitude from the two-wave superposition is given as $\sqrt{I} = \sqrt{I_{KN}} - \sqrt{\delta I}$.

The above iterative procedure can be summarized in flow chart Fig. 1 and the Algorithm

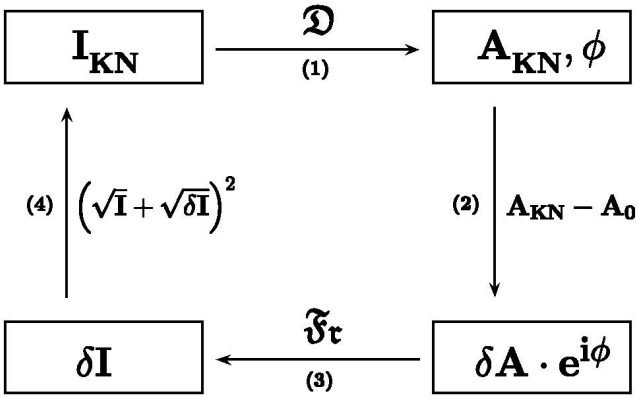

Fig. 1. Flow chart of APBA

Algorithm. *In an imaging experiment, assume we have performed two imaging measurements. One image (radiograph) is the attenuation image A_0^2 acquired at SID= R_1, another is a normalized phase-contrast image $I = M^2 \cdot I_D(\vec{r}_D)/I_{\text{in}}$ acquired at SID= $R_1 + R_2$. With A_0^2 and I as well as the initial δI, usually 0, as known inputs, we first assume $I_{\text{KN}} = \left(\sqrt{I} + \sqrt{\delta I}\right)^2$. Then*

(1). *Compute $A_{\text{KN}} = \sqrt{\mathfrak{D}(I_{\text{KN}})}$ and ϕ from the duality transform Eq. (6).*

#126430 - $15.00 USD Received 2 Apr 2010; revised 11 Jun 2010; accepted 9 Jul 2010; published 15 Jul 2010

(2). *Compute* δA *from*

$$\delta A = A_{\mathrm{KN}} \cdot (1 - P), \qquad P = A_0 / A_{\mathrm{KN}}. \tag{10}$$

Equations (9) and (10) are in fact the same equations. The advantage of Eq. (10) over (9) is that we can set a threshold for P. We know $P = A_{\mathrm{pe,coh}}$ *in the ideal case and* $A_{\mathrm{pe,coh}}$ *is bounded between* 1 *and* A_0*. The computation rounding error or the presence of measured noise in the acquired data can make the value of P over pass these bounds in the iterative computations. By setting a threshold upper bound* $\mathrm{ubd} = 1$ *and lower bound* $\mathrm{lbd} = \min(A_0)$*, the minimum value of* A_0*, to P in the iterative computations, we can make the algorithm more stable. Moreover, if we know a better* lbd *for* $A_{\mathrm{pe,coh}}$*, other than the minimum of* A_0*, the converging speed of the algorithm can be greatly improved.*

(3). *Compute* δI *by Fresnel propagate* $\delta A e^{i\phi}$ *from position* R_1 *to* R_2*:* $\delta I = \left|\mathfrak{F}_{\mathfrak{r}}\left(\delta A e^{i\phi}\right)\right|^2$ *with*

$$\mathfrak{F}_{\mathfrak{r}}(T)(\vec{r}) = \frac{1}{\lambda R_2} \int_{\mathbb{R}^2} \exp\left[i \frac{\pi M}{\lambda R_2} \left(\frac{\vec{r}}{M} - \vec{\xi} \right)^2 \right] T(\vec{\xi}) d\vec{\xi}. \tag{11}$$

(4). *Compute* $I_{\mathrm{KN}} = \left(\sqrt{I} + \sqrt{\delta I}\right)^2$*. Go to* (1) *for next iteration.*

The number of iterations or an accuracy measure can be used to determine when to exit the program: assuming $\|\cdot\|$ is some kind of norm, that can effectively reflect the accuracy of the retrieved data as an image, if $\|\delta I_{k+1} - \delta I_k\|$ is less than a predefined threshold value β, or the iteration step exceeds a predefined maximum number of iteration steps, then ϕ is the retrieved phase and the iteration stops; otherwise further iteration is needed.

An appropriate image accuracy measure should be a measure that can effectively reflect the accuracy of the data AND at the same time correctly reflect the visual perception of the data as an image, since an image's visual perception is crucial for diagnostic radiology. In the next subsection the authors suggest a measure which can be employed as an appropriate image accuracy measure, which was first investigated by Rudin in [32].

2.2. *An Image Accuracy Measure*

(a) (b) (c)

Fig. 2. Example "Lena" images used in measuring the closeness between images. (a) ϕ_1, (b) ϕ_2, (c) ϕ_3

A continuous signal is generally represented as a function of vector variables: $f(\vec{\mathbf{r}})$. A sampled signal will be represented as a one- (or higher) dimensional sequence of real numbers. In

#126430 - $15.00 USD Received 2 Apr 2010; revised 11 Jun 2010; accepted 9 Jul 2010; published 15 Jul 2010

this paper, we will denote the continuous two dimensional image as an intensity function of two dimensional variables, such as $f(x,y)$, or $f(\vec{\mathbf{r}})$, $\vec{\mathbf{r}} = (x,y)$. The sampled 2-D image will be represented by $f(i,j)$, $i = 1,2,\cdots,m$, $j = 1,2,\cdots,n$. In practice, to estimate a true signal in noise, the most frequently used methods are based on the least squares criteria and thus an intuitive measure for the closeness of two image functions f and g is, similar to statistical standard deviation, based on:

$$\mathrm{std}(g,f) := \frac{\left[\int_\Omega \left(g(\vec{\mathbf{r}}) - f(\vec{\mathbf{r}}) - \mu\right)^2 d\vec{\mathbf{r}}\right]^{1/2}}{V(\Omega)}, \tag{12}$$

where Ω is the finite domain of image functions f and g, $V(\Omega)$ represents the area of domain Ω, and $\mu = \int_\Omega (g-f)d\vec{\mathbf{r}}/V(\Omega)$ is the statistical mean value of $g-f$. In [32], L. I. Rudin investigated the relation of edge formation of the 2-D digital image and the singularities of the image function and pointed out that the image intensity function belongs to the space of functions of bounded total variation. Rudin et al.[33] pointed out that the proper norm for images is the total variation (TV) norm, which is the L_1 norm of the gradient of the image function, and not the L_2 norm. For two image functions f and g, we define the TV norm of $g-f$ as the closeness of the two images:

$$\mathrm{TV}(g,f) := \frac{\int_\Omega |\nabla(g-f)|\, d\vec{\mathbf{r}}}{V(\Omega)} = \frac{\int_\Omega \sqrt{\left(\frac{\partial(g-f)}{\partial x}\right)^2 + \left(\frac{\partial(g-f)}{\partial y}\right)^2}\, d\vec{\mathbf{r}}}{V(\Omega)}, \tag{13}$$

where ∇ is the gradient operator. Since std is the form of L_2 norm, it is not suitable as a measure to represent the closeness between two images. For example, for the three "Lena" image functions shown in Fig. 2, the std measures of $\phi_1 - \phi_2$ and $\phi_1 - \phi_3$ are $\mathrm{std}(\phi_1,\phi_2) = 0.206$, $\mathrm{std}(\phi_1,\phi_3) = 0.472$ respectively. But the image ϕ_3 is much more closer to ϕ_1 than ϕ_2 does in visual perception. This is because the digital representation of an image depends not only on the pixel values, it also depends on the contrast changes between neighbor pixels. An image's visual perception is crucial for diagnostic radiology. This contrast changes between neighbor pixels can better be represented by the gradient changes of the image functions. For example, the TV measures of $\phi_1 - \phi_2$ and $\phi_1 - \phi_3$ are $\mathrm{TV}(\phi_1,\phi_2) = 0.0247$ and $\mathrm{TV}(\phi_1,\phi_3) = 0.0138$ respectively, more appropriate in reflecting the visual perception. In this paper, we will use the TV norm (13) as the measure for closeness between two compared image functions.

Note that the TV norm between two image functions, say g and f, equals 0 if and only if g differs from f by a constant. This feature does not affect its appropriateness for phase retrieval since it is well known that the recovered phase ϕ is unique up to a constant with given information about the attenuation-map A_0 and the phase-contrast intensity-map I.

3. Simulation Tests

In order to investigate the performance of the algorithm constructed above, we perform computer simulations in this section. In Section 3.1, we first construct a breast tissue model that represents the phase-shifts and attenuation of breast tissues and embedded microcalcifications for different x-ray energies. In our simulation tests, the distances of source point to object, R_1, and object to detector, R_2, are set to 26 inches (0.66 m) respectively. In this way the magnification factor $M = (R_1 + R_2)/R_1$ is equal to 2. For convenience, the incident x-ray intensity I_{in} at R_1 is set to M^2 (4). We compare the performance of our algorithm, APBA, with two other widely used algorithms: the Gerchberg-Saxton (GS) algorithm (Section 3.2) and the TIE algorithm (Section 3.3).

#126430 - $15.00 USD Received 2 Apr 2010; revised 11 Jun 2010; accepted 9 Jul 2010; published 15 Jul 2010

3.1. A breast specimen model

The tissue's phase-shift and attenuation are determined not only by the tissue's physical composition, but also by the x-ray energy. With different x-ray energy, the same tissue has different phase-shift and attenuation change. Simulation models used in literature often do not incorporate these changes. In this subsection, we construct a breast specimen model that can represent tissue attenuation and phase shifts according to employed x-ray energies as well as tissue's compositions.

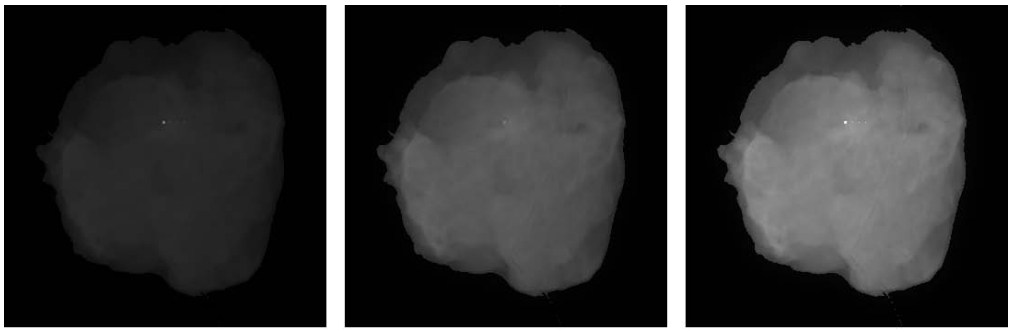

(a) (b) (c)

Fig. 3. Image manifest of (a) $A^2_{\text{pe,coh}}$, (b) A^2_{KN} and (c) A^2_0 when x-ray energy equals 35.5 keV.

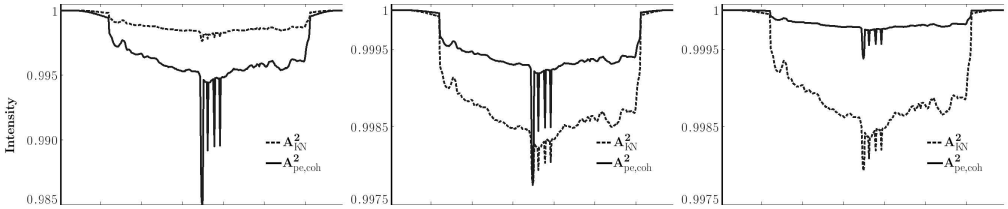

(a) (b) (c)

Fig. 4. Profiles of $A^2_{\text{pe,coh}}$, the solid lines, and A^2_{KN}, the dotted lines, when x-ray energy equals (a) 18.5 keV, (b) 35.5 keV and (c) 59.5 keV.

In our model the tissue has two physical compositions: the 50% glandular-50% adipose breast tissue and the microcalcifications. In order to simulate the morphological aspects of breast tissues, we adopted a radiograph of a breast lumpectomy specimen with pixel values rescaled and the metal localization wire removed by replacing the pixel value at wire position with a mean pixel value at near by positions. It is difficult to remove all the residual trace of the wire this way as can be seen from the following image display especially for the phase contrast image (Fig. 5(c)). In the phase contrast image (Fig. 5(c)), the small residual variation from the original wire-track really got enhanced. The linear attenuation coefficients and electron densities for the 50% glandular-50% adipose breast tissues are computed from the tissue's elemental composition and the interpolated elemental mass attenuation coefficients from the standard reference in the mammographic radiation dosimetry [34, 35]. Moreover, each mass attenuation coefficient is further broken down to two components: one from x-ray photoelectric absorption and coherent scattering, and another from incoherent scattering. In this way, the total attenuation is partitioned as a product of $A^2_{\text{pe,coh}}$ and A^2_{KN} as defined in Eq. (8) above.

#126430 - $15.00 USD Received 2 Apr 2010; revised 11 Jun 2010; accepted 9 Jul 2010; published 15 Jul 2010

In addition, to simulate the microcalcifications in breast, four small ellipsoids of calcium carbonate (CaCO3) are embedded in the specimen model. The diameter of the ellipsoids can be adjusted in simulating different size of the microcalcifications. In the following simulations, to test phase-contrast sensitivity, we set the diameters of the four ellipsoids to 10, 5, 10, and 5 microns in x-ray direction and 300, 200, 300, 200 microns in detector plane respectively.

The attenuation image A_0^2 of the specimen model simulated with 35.5 keV x-ray, and its two corresponding partition images A_{KN}^2 and $A_{\mathrm{pe,coh}}^2$, are shown in Fig. 3. For a comparison, the profiles of A_{KN}^2 and $A_{\mathrm{pe,coh}}^2$ along the line passing through the microcalcifications are shown in Fig. 4 simulated with x-ray energy equals 18.5, 35.5 and 59.5 keV, respectively. We can see that the contribution of $A_{\mathrm{pe,coh}}^2$ to the total attenuation A_0^2 gets smaller when x-ray energy is getting higher. Especially, when x-ray energy equals 59.5 keV, the contribution of $A_{\mathrm{pe,coh}}^2$ for the soft tissue can almost be neglect, as is expected.

3.2. Comparison with the GS Algorithm

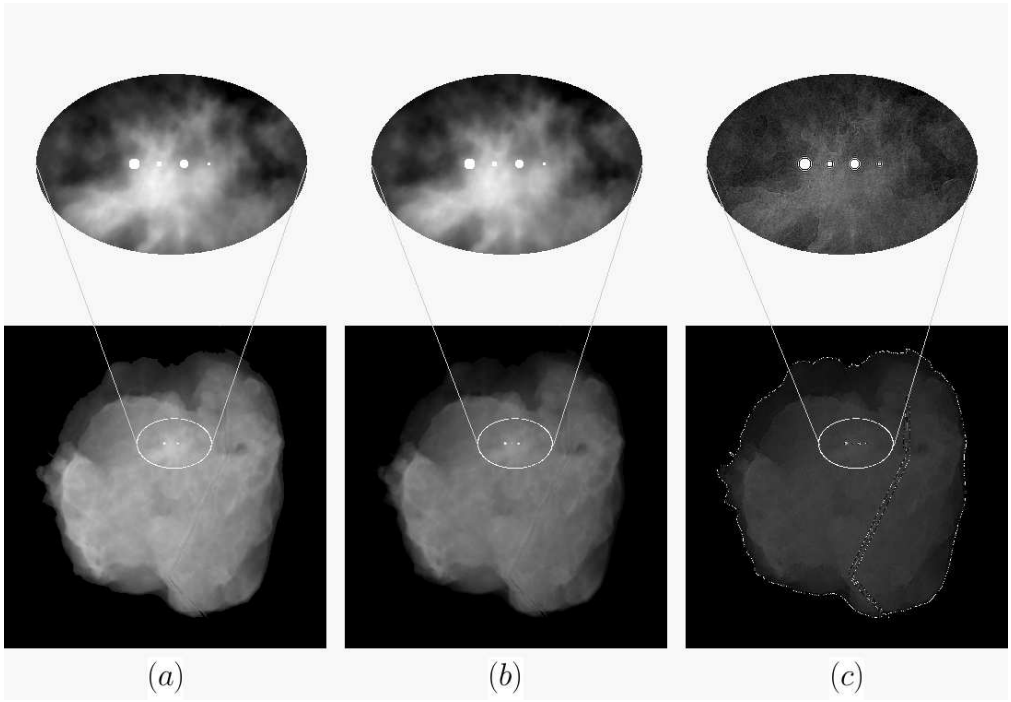

Fig. 5. Image representation of the inputs generated from the simulation model and Fresnel propagation. (a) the phase map ϕ; (b) the attenuation map A_0^2; and (c) the normalized Fresnel propagated phase contrast image I with object to detector distance $R_2 = 26$ in (0.66 m).

The GS algorithm is an iterative algorithm for phase retrievals from a pair of images at two planes related by the Fourier transform. For details readers are referred to [26]. The GS algorithm is a classical algorithm which is widely used in electron microscopy, wave front sensing, astronomy, crystallography, and many other fields involving phase recovery [27, 28, 36].

By replacing the Fourier Transform in the GS algorithm with the Fresnel transform of Eq. (11), we get a modified version of the GS algorithm extended to the *Fresnel diffraction regime*. Our previous simulation tests showed that this modified GS algorithm converges very

#126430 - $15.00 USD Received 2 Apr 2010; revised 11 Jun 2010; accepted 9 Jul 2010; published 15 Jul 2010

slow for object-detector distance $R_2 \approx 1\,\mathrm{m}$, and converges faster for larger R_2, such as images acquired at synchrotron beam lines. But this is generally not applicable to the field of clinical imaging, due to the physical constraints such as compact sizes of hospital rooms.

In our simulation tests, we compare the performance of APBA and that of the GS algorithm. The photon energy of the point x-ray source is set to 35.5 keV, and the distances from the source to object and object to detector are set to $R_1 = R_2 = 26$ inches (0.66 m) respectively. For convenience, the incident x-ray intensity I_{in} at R_1 is set to M^2, where $M = (R_1 + R_2)/R_1$ is the magnification factor. The phase map ϕ and the attenuation A_0^2 are generated from our phantom model for 35.5 keV x-ray. Fig. 5 shows the simulated images of the phase map ϕ, the attenuation image A_0^2 and the phase-contrast image I.

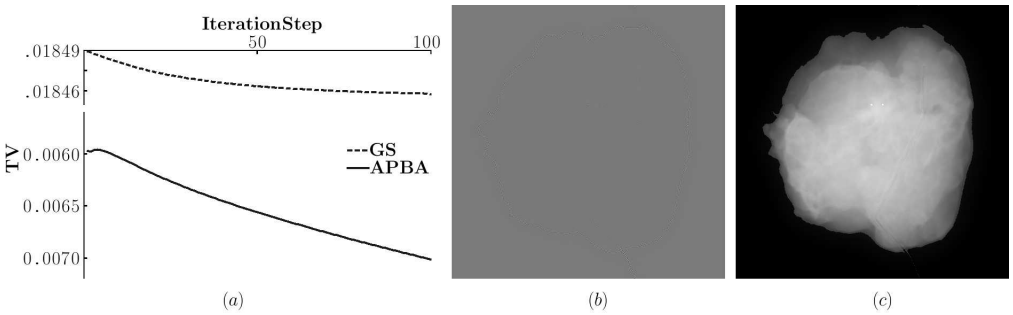

Fig. 6. Comparison of the performance of the GS algorithm and APBA. (a) plot of the accuracy measures with respect to iteration steps. The plot with solid line represents the APBA. The one with dashed line represents the GS algorithm; (b) recovered phase map with the GS algorithm after 100 iterations; (c) recovered phase map with APBA after 100 iterations.

In the simulation test, the iteration for our attenuation-partition based algorithm (APBA) and the GS algorithm are performed 100 steps. The corresponding recovered phase images are shown in Fig. 6(b) and (c). In Fig. 6(a), the solid line represents the change of total variation (TV) of the retrieved phase using attenuation-partition based algorithm with respect to the iteration steps. The dashed line represents the change of TV of the retrieved phase using the (modified) GS algorithm with respect to iteration steps. We can see that the converging speed of the (modified) GS algorithm is much slower than that of attenuation-partition based algorithm (the change of TV of APBA from step 1 to step 100 is $1.04E-3$, almost 33 times greater than that, $3.17E-5$, of the GS algorithm.) In addition, from the visual perception point of view, we see that the phase map retrieved with the attenuation-partition based algorithm (APBA) is much better than that retrieved with the (modified) GS algorithm.

The main difference between APBA and the GS algorithm is that APBA takes the advantage of the phase-attenuation correlation property, although the extent of this correlation is not known in *priori*, but the GS algorithm does not. From this example we see that the phase-attenuation correlation is a very important information that shouldn't be neglected in the algorithm development for phase retrieval.

3.3. Comparison with the Transport of Intensity (TIE) algorithm

We have mentioned the transport of intensity equation in Eq. (3) in Section 1. Since Teague proposed the TIE algorithm for phase retrieval in 1983 [21], numerous phase retrieval algorithms have been suggested on how to effectively search the numerical solution of the TIE [4, 20, 25, 37, 38, 39, 40]. Among the methods of solving the above TIE for the phase map, the one based on Fast Fourier Transform, proposed by Nugent et al. [4], and Allen and Oxley

#126430 - $15.00 USD Received 2 Apr 2010; revised 11 Jun 2010; accepted 9 Jul 2010; published 15 Jul 2010

in [25], is the most widely used. In the form of pseudo-differential operator, the solution phase map ϕ is given by

$$\phi(\vec{\mathbf{r}}) = -\frac{2\pi M}{\lambda R_2}\nabla^{-2}\left\{\nabla\cdot\left[\frac{\nabla\left[\nabla^{-2}\left(I-A_0^2\right)\right]}{A_0^2}\right]\right\}, \tag{14}$$

for the given normalized phase-contrast image I and attenuation image A_0^2. Here ∇ is the gradient operator, and ∇^{-2} is the inverse Laplacian operator.

The advantage of this algorithm is that it does not require the boundary information in solving the TIE (assuming the image data is periodic); it is a deterministic method and thus the algorithm is fast and accurate comparing to most iterative algorithms. In this section we compare the performance of the TIE algorithm and that of APBA for two kind of cases: first for the ideal case without any noise and any image misalignment, then for cases simulating practical situation with x-ray imaging noise and possible image misalignment. In these simulation tests, the imaging geometries are the same as in the previous subsection, and x-ray energy is again 35.5 keV .

For the ideal case without any noise and any image misalignment, the performance comparison results are shown in Fig. 7. For the ideal case the TIE algorithm is accurate both in TV measure and visual perception. APBA can also achieves this accuracy but needs 1110 iteration steps to have its TV measure of 0.00215226, an error smaller than that of 0.00215269 with the TIE algorithm.

However, the real test lies in the performance for the cases simulating practical situation with x-ray imaging noise and possible image misalignment. Obviously only the performance in these cases really matters in phase contrast imaging applications, especially for clinical imaging applications where the imposed radiation limits dictates existence of substantial x-ray quantum noise in acquired images. Implemented in the Fourier space, the inverse Laplacian ∇^{-2} in Eq. (14) is singular at zero spatial frequency. This singularity will amplify the noise in the images and result in failure of accurate phase retrieval for the TIE algorithm. To overcome this difficulty, some kind of regularization must be used. The most widely used regularization is Tikhonov regularization, which replaces ∇^{-2} by $|\vec{\mathbf{u}}|^2/(|\vec{\mathbf{u}}|^4+\kappa^2)$, for some "favorable" constant parameter κ, called the Tikhonov regularization parameter. In this regularization scheme, the singularity is regularized, and the favorable parameter κ means the retrieved phase ϕ_κ corresponding this κ is as close to the true phase ϕ as possible. Roughly speaking, the regularization

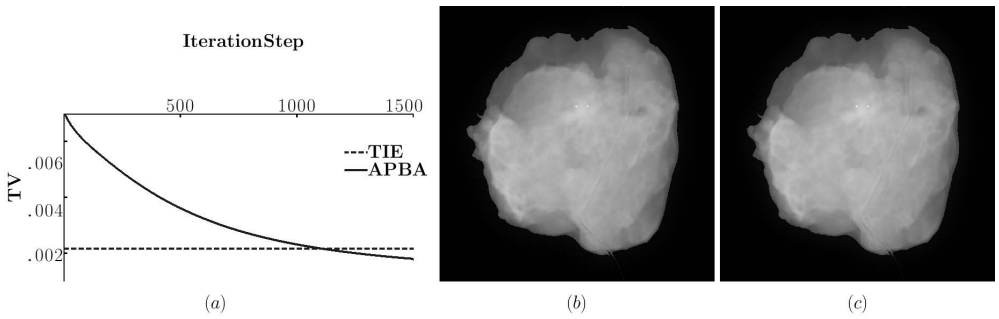

Fig. 7. Comparison of APBA and the TIE algorithm with pure data. (a) plot of the accuracy measure with respect to iteration steps. The plot with solid line represents the APBA. The one with dashed line represents the TIE algorithm. It needs 1110 steps for the TV measure, 0.00215226, of APBA to achieve to the TV measure, 0.00215269, of TIE; (b) recovered phase using the TIE algorithm; (c) recovered phase using APBA after 1500 iteration steps.

#126430 - $15.00 USD Received 2 Apr 2010; revised 11 Jun 2010; accepted 9 Jul 2010; published 15 Jul 2010

parameter κ is inversely proportional to the images signal-noise ratio. Two problems, however, arise to this regularization. First, the true phase ϕ is not known in real situations. So the regularization parameter κ is not a priori, which makes it difficult in practical applications. Second, this Tikhonov regularization is based on finding a stable solution to $Ax = y$, in Hilbert spaces X, Y, by solving the minimization problem

$$x_\kappa = \arg\min_{x \in X} \|Ax - y\|_Y^2 + \kappa \|x\|_X^2 . \tag{15}$$

It is L_2 norm dependent. Since the proper norm for image data is the total variation (TV) norm [33], a favorable solution under the Tikhonov regularization principle can not be guaranteed a best solution in visual perception. Moreover, for relatively noisy acquired images, the TIE-based algorithm, even with Tikhonov regularization, often failed to retrieve the phase maps[1].

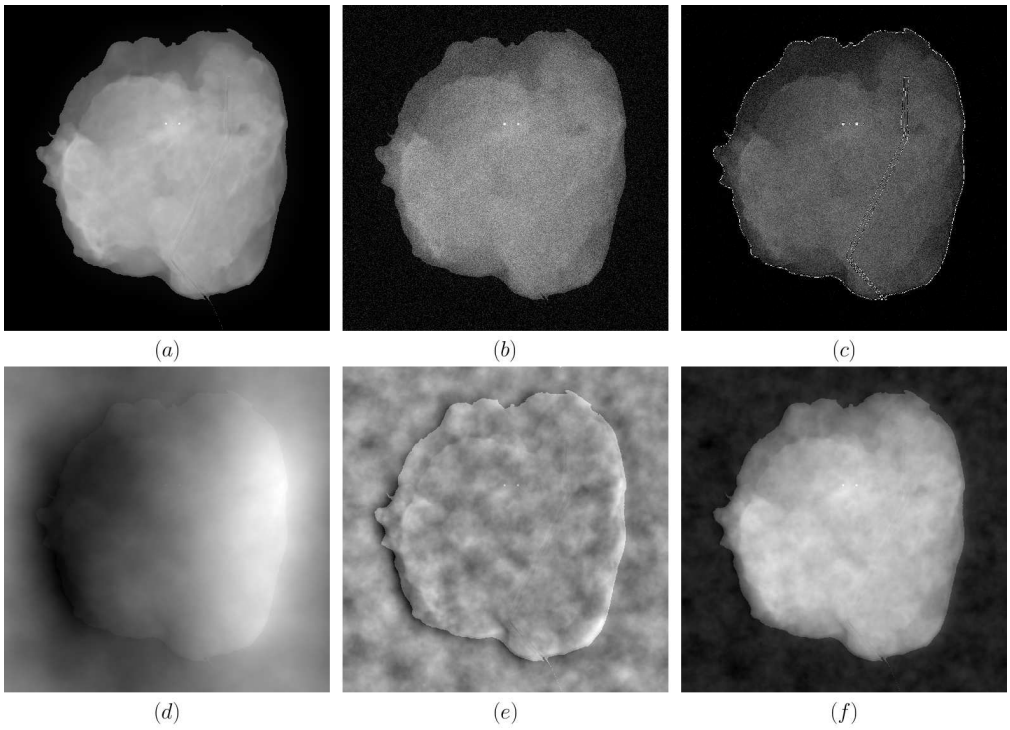

Fig. 8. Comparison of the TIE algorithm and APBA with noise added. (a) True phase map ϕ; (b) attenuation map A_0^2; (c) the normalized phase contrast image I; (d) recovered phase map with the TIE algorithm, no Tikhonov regularization is used; (e) recovered phase map with the TIE algorithm with Tikhonov regularization; (f) recovered phase map with APBA after 10 iteration steps. In the simulation, the acquired data is assumed to have a level of $\delta_b = 0.03\%$ detector noise and one pixel misalignment between A_0^2 and I horizontally.

In the following, we will compare the performance of APBA and the TIE-algorithm when noise is present. In the practice of phase retrieval, there are generally two kinds of image data errors. One is the noise associated with image acquisitions, including the quantum noise of x-ray photon detections and detector electron noise. We assume the quantum noise dominates as is the case in most imaging applications. The other is the error caused by the misalignment between the attenuation map A_0^2 and phase-contrast image I. This is because usually the attenuation image and corresponding phase contrast image are generally acquired in two separate x-ray

#126430 - $15.00 USD Received 2 Apr 2010; revised 11 Jun 2010; accepted 9 Jul 2010; published 15 Jul 2010

exposures. The misalignment could be resulted from the shift or tilting of the object or detector between the exposures. In the simulation, we associate each pixel value of an image a photon count N, so that $P(i,j) = c \cdot N(i,j)$, where c is a constant. Assuming the noise has a Poisson distribution, with variance $\sigma^2 = N$ at each pixel. In the simulation we assign a background noise level for each simulated image. This background noise level is defined as the ratio $\delta_b = \sigma_b / N_b$ corresponding to the direct exposure area (where $A^2 = 1$) outside the object in background. The Poisson statistics dictates that $N_b = 1/\delta_b^2$ and in this way the photon count $N(i,j)$ can be determined accordingly at each pixel. Once $N(i,j)$ is determined, the statistical errors at each pixel can be assigned using a computer simulated random Poisson distribution generator with mean corresponding to the photon counts $N(i,j)$. In the simulations below, the background noise level δ_b is set to 0.0003. The images with the noise added are shown in Fig. 8(b) and (c). The quality of an image depends not only on the noise level but also on the extent of image contrast change. With the assumption $P(i,j) = c \cdot N(i,j)$ above, one can easily see that $\delta_b = \sigma_{P_b}/\overline{P_b}$ is the statistical coefficient of variation in absorbed photon numbers in background. $\delta_{oi} = \sigma_{P_{oi}}/\overline{P_{oi}}$, the coefficient of variation of the object image, on the other hand, is the structural coefficient of variation of the sampled image, which reflects the image's normalized extent of image contrast change. We will use the ratio δ_{oi}/δ_b to reflect the image quality. The larger the ratio, the higher the image quality. In our simulation models, when $\delta_b = 0.0003$, the corresponding ratio δ_{oi}/δ_b for attenuation A_0^2 and phase-contrast image I, Fig. 8(b) and (c), are 1.67 and 6.35 respectively. Because of the phase-contrast effect, the image quality of the phase-contrast image I is higher than the attenuation image A_0^2 although they have the same background noise level.

Three simulation tests are performed in the comparison: case1: assume the acquired data A_0^2 and I has noise present but perfectly aligned; case 2: assume acquired data has no noise but has one pixel misalignment horizontally; case 3: assume acquired data has combined detector noise as well as one pixel misalignment. One bias in simulation for the TIE-algorithm should be mentioned: with the known true phase value, a favorable Tikhonov regularization parameter κ can be searched, but in practice this search is hardly feasible. In each case mentioned above, three phase retrievals are performed: 1. using the TIE-algorithm without Tikhonov regularization; 2. using the TIE-algorithm and the favorable Tikhonov regularization parameter; 3. using APBA with 10 step iteration. The Total variation (TV) of the results are listed in Tab. 1 and the recovered phase images for case 3 are shown in Fig. 8(d) – (f). The results using Tikhonov regularization are better than those not using Tikhonov regularization but worse than those using APBA. The influence of misalignment to APBA is little but disaster to the TIE algorithm. From the profile, shown in Fig. 9, along a line passing through the microcalcifications we can see that the values of the phase recovered from APBA is very close to the true phase value, but the values of the phase recovered from the TIE algorithm are distorted.

4. Discussion and Conclusion

Table 1. TV comparison of the TIE algorithm and APBA. In the table, κ is the Tikhonov regularization parameter, Δ represents the sampling step-size in FT-space.

	TV =		
	Case 1	Case 2	Case 3
TIE: no Tikhonov	0.0406	0.0808	0.0886
	$\kappa = 0.7828\Delta^2$	$\kappa = 4.4421\Delta^2$	$\kappa = 4.1076\Delta^2$
TIE: with Tikhonov	0.0399	0.153	0.0379
APBA	0.0283	0.0086	0.0290

#126430 - $15.00 USD Received 2 Apr 2010; revised 11 Jun 2010; accepted 9 Jul 2010; published 15 Jul 2010

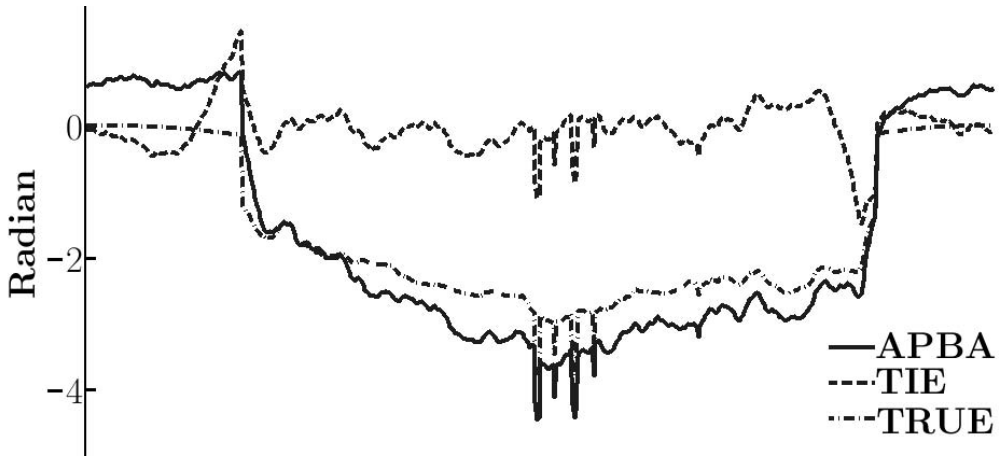

Fig. 9. Profiles, along a line passing through the microcalcifications, of the recovered phase using APBA, the solid line, and using the TIE algorithm with Tikhonov regularization, the dashed line, in Case 3. The dash-dotted line is the true phase.

In above analysis, we assumed that the x-ray source is a quasi-monochromatic point source. In practice, one often employs conventional incoherent and polychromatic sources such as x-ray tubes for imaging. In the experiments with an x-ray tube source, the previous formula Eqs. (2–3) of the phase contrast image intensities should be modified. Since in the APBA method the duality transform is derived based on Eq. (3), hence the Eq. (6) should be modified accordingly. In our previous works we have studied this problem [20]. With the Wigner function based phase space formalism, we have proved that the coherence degree of a finite-size focal spot can be accounted for by the optical transfer function $OTF_{G.U.}(\vec{u}/M)$ for the geometrical unsharpness associated with the finite-size source [20]:

$$OTF_{G.U.}\left(\frac{\vec{u}}{M}\right) = \frac{\int I_{\text{spot}}(\vec{\xi}) \exp\left[i2\pi\vec{\xi}\cdot\frac{(M-1)\vec{\mathbf{u}}}{M}\right] d\vec{\xi}}{\int I_{\text{spot}}(\vec{\xi}) d(\vec{\xi})}$$

where $I_{\text{spot}}(\vec{\xi})$ is the intensity distribution of the focal spot. We found the generalized TIE equation with an x-ray tube source, that is, the x-ray intensity at the detector is given by [20]:

$$I(\vec{\mathbf{r}}; R_1+R_2) = \frac{I_{\text{in}}}{M^2}\mathscr{F}^{-1}\left(OTF_{G.U.}\left(\frac{\vec{\mathbf{u}}}{M}\right)\right) \otimes \left\{A^2\left(\frac{\vec{\mathbf{r}}}{M}\right) - \frac{R_2\langle\lambda^2\rangle}{2\pi M\langle\lambda\rangle}\nabla\cdot\left(A^2\nabla\phi\left(\frac{\vec{\mathbf{r}}}{M}\right)\right)\right\},$$

where operator $\otimes$ denotes the convolution, A^2 is the total attenuation of the imaged object, ϕ is the spectrally averaged phase-shift caused by the object, and $\langle\cdot\rangle$ means the spectral average. Compare above equation with Eq. (3) and it is clear that the TIE-based phase retrieval method needs only two modifications: (i). Fourier space de-convolution of the measured intensity from $OTF_{G.U.}(\vec{u}/M)$, (ii). Replacing wavelength with the spectral-averaged $\langle\lambda^2\rangle/\langle\lambda\rangle$. In the same fashion, the duality transform $\mathfrak{D}$ defined in Eq. (6) should be modified with (i). Fourier space de-convolution of the measured intensity from $OTF_{G.U.}(\vec{u}/M)$; (ii). A replacement of the parameter $\tilde{k}$ defined in Eq.(7) with the spectral-average

$$\langle\tilde{k}\rangle = \frac{r_e R_2}{2\pi M}\cdot\left\langle\frac{\lambda^2}{\sigma_{\text{KN}}}\right\rangle.$$

#126430 - $15.00 USD Received 2 Apr 2010; revised 11 Jun 2010; accepted 9 Jul 2010; published 15 Jul 2010

Otherwise, the APBA flow chart is the same as that for the case with a quasi-monochromatic point source.

Phase retrieval is a crucial step for quantitative imaging such as reconstructing the 3-D distribution of tissue linear attenuation coefficients and refraction indices. However, images acquired in medical applications are relatively noisy, due to the radiation dose constraints, with low phase contrast effect, due to physical constraints such as compact sizes of hospital rooms. An phase retrieval algorithm which is robust to noise is necessary for potential medical phase contrast imaging. In [1], the authors developed an algorithm, called attenuation-partition based phase retrieval algorithm. It is an iterative algorithm which takes advantage of the correlation between the attenuation and phase-shift. The phase retrieval results from experimental images show that this algorithm is fast and robust [1]. In this work, we systematically compared the performance of this algorithm with other two widely used phase retrieval algorithms, namely the Gerchberg-Saxton (GS) algorithm and the Transport of Intensity Equation (TIE) algorithm. The systematical comparison is conducted by analyzing phase retrieval performances with a digital breast specimen model. We show that the proposed algorithm converges faster than the GS algorithm in the Fresnel diffraction regime, and is more robust against image noise than the TIE algorithm. These results suggest the significance of the proposed algorithm for future medical applications with the x-ray phase contrast imaging technique.

Acknowledgements

This research was supported in part by the Department of Defense Breast Cancer Research Program under award number W81XWH-08-1-0613 and the NIH grant 1R01CA142587.

#126430 - $15.00 USD Received 2 Apr 2010; revised 11 Jun 2010; accepted 9 Jul 2010; published 15 Jul 2010

processed using two algorithms to localize events: (i) simple-threshold and (ii) weighted-centroid methods. The processed frames were added to give the final image. **Results:** (i) Stationary collimator: The image showed a grid-like pattern corresponding to the septa walls of the collimator. All of the hot rods in the phantom can be identified. (ii) Moving collimator: The septal pattern is blurred out, and all of the rods can be clearly identified. **Conclusion:** The same MAF can be used in both nuclear-medicine imaging and x-ray imaging in SPC mode for dual-mode imaging. Currently we are limited by collimator resolution for radionuclide imaging. Support from: NIH Grants R01EB002873 and R01EB008425.

MO-E-204C-02

Bedside SPECT Imaging with Pinhole Collimation

A Cebula[1] *, D Gilland[1], M Studenski[2], (1) University of Florida, Gainesville, FL, (2) Thomas Jefferson University, Philadelphia, PA

Purpose: The objective of this study is to evaluate the imaging performance of a mobile SPECT system with a pinhole collimator and compare the results with parallel hole collimators. The goal is to obtain both planar and tomographic performance measures with Tc-99m and F-18. This abstract presents the results using Tc-99m. **Method and Materials:** The system utilizes a small field of view camera with pixilated NaI crystal and position-sensitive photomultiplier tubes. The pinhole collimator is a tungsten knife edge with a hole diameter of 3mm, a focal length of 12.5cm, and an acceptance angle of 90 degrees. The parallel hole collimators have been previously described along with their imaging performance evaluation [1]. The following performance measures with the pinhole collimator were obtained and are presented here: count rate performance, energy resolution, flood field uniformity, system spatial resolution, system sensitivity. **Results:** The maximum count rate was calculated to be 1.58×10^5 cps corresponding to an activity of 161 μCi at 30cm. An energy spectrum from the flood acquisition demonstrated an energy resolution of 20% FWHM. Magnification corrected, system planar spatial resolution was 1.03 cm with a system sensitivity of 1.39 cps/μCi at a source to collimator distance of 10 cm. **Conclusion:** The imaging performance of a mobile SPECT system with a pinhole collimator has been presented. In comparison to parallel hole collimation, the pinhole collimator provides superior spatial resolution and sensitivity at distances less than 5cm. However, at further distances, pinhole sensitivity declines while parallel hole sensitivity remains relatively constant.

Research sponsored by the United States Army Medical Research and Material Command under Award No. W81XWH-04-1-0594

MO-E-204C-03

On the Development of On-Board PET with Tomotherapy Using Open Dual Ring Geometry

N Darwish[1] *, T Mackie[2], B Thomadsen[3], C Kao[4], (1) University of Wisconsin, Madison, WI, (2) University of Wisconsin - ADCL, Madison, WI, (3) University of Wisconsin, Madison, WI, (4) Univ Chicago, Chicago, IL

Purpose: Positron emission tomography (PET) using open dual ring geometry was investigated as an on-board system for functional imaging and PET marker tracking, specifically with tomotherapy. The dual ring PET would allow measurement of both inter and intra-fractional variation, facilitating the determination of treatment uncertainties and improving the delineation of tumor volume at any stage in the radiation treatment delivery process. This study demonstrates the field of view (FOV) of various PET ring axial gaps, the sensitivity of each system for each gap, and the image quality as a function of scan time and activity for one specified design. **Method and Materials:** Investigation of FOV and sensitivity of each design was accomplished via Monte Carlo simulations with GATE, the Geant4 Application for Emission Tomography. Image quality was investigated with a fully 3D OSEM iterative reconstruction algorithm for noiseless data to investigate the FOV and noisy data to investigate the scan time at a specified activity. **Results:** Even when the axial gap (G) exceeded the axial width (W) for each open ring system as in the extreme case of G = 600 mm (required to avoid actuators holding MLC's) the axial FOV was approximately 200 mm. A continuous axial and transaxial FOV (determined by PET ring diameter) of 360 mm and 450 mm respectively resulted from G=W=120mm. Reconstructed NEMA 2001 phantom images for activity of 15 mCi/70kg and scan times ranging from 10 to 100 seconds was demonstrated without the effect of attenuation, scatter, and random events. **Conclusion:** For tomotherapy treatment 200 mm continuous FOV axially was sufficient and was achievable with all gaps simulated in the range from 120 mm to 600 mm. Open dual ring on-board PET has the potential to acquire images within the time limit of a tomotherapy treatment session.

MO-E-204C-04

Improving Robustness of Phase Retrieval in X-Ray Phase Contrast Imaging

X Wu[1] *, A Yan[1], H Liu[2], (1) Univ Alabama Birmingham, Birmingham, AL, (2) Univ Oklahoma, Norman, OK

Purpose: The phase retrieval, retrieving tissue phase maps from the x-ray phase contrast images, is an important task in x-ray phase-sensitive imaging. The robustness of phase retrieval algorithms is of critical importance for reducing radiation doses in clinical applications. We show that the conventional phase retrieval method is actually unstable against the quantum noise. We present a more robust phase retrieval method that we developed. **Method and Materials:** We first studied the phase retrieval by means of the conventional Transport of Intensity Equation (TIE) method for phantom imaging (such as a nylon air bubble wrap). For improvement we developed a robust phase retrieval method based on our notion of the phase–attenuation duality and attenuation partition, and derived a robust iterative phase retrieval algorithm. This algorithm had been applied to experimental phase contrast imaging with phantoms. In addition the phase retrieval accuracies had been analyzed with computer simulations of phase contrast imaging of a digital phantom of breast tissue characteristics. **Results:** We found that the TIE-based phase-retrieval suffers from an intrinsic singularity**.** The phantom imaging showed that the TIE-based phase retrieval method is unstable against the noise and misalignment in phase contrast imaging, even if the Tikhonov regularization was employed. In contrast, our method based on the phase–attenuation duality and attenuation partition is singularity-free, and is robust in terms of the phase-map image quality and phase-map accuracies against the noise and misalignment, as is verified by means of experimental phantom imaging and computer simulation. **Conclusion**: The conventional TIE-based phase retrieval method is unstable against noise and image misalignment. Our phase retrieval method method based on the phase–attenuation duality and attenuation partition is robust against the noise and image misalignment.

Research supported in part by DoD Breast Cancer Research Program.

MO-E-204C-05

X-Ray Luminescence Computed Tomography Via Selective X-Ray Excitation

G Pratx*, C Carpenter, C Sun, L Xing, Stanford University School of Medicine, Stanford, CA

Purpose: X-ray luminescence computed tomography (XLCT) is proposed as a new molecular imaging modality for imaging X-ray-excitable phosphorescent nanoparticles three-dimensionally, in living subjects. Some of these nano-sized particles can emit near-infrared (NIR) light when excited with X rays and are particularly well suited for in-vivo biomedical imaging because the signals can propagate long distances in tissue. **Method and Materials:** The imaging mechanism used in XLCT consists in irradiating the subject using a sequence of programmed X-ray beams, while sensitive photo-detectors measure the light coming out of the subject. By restricting the X-ray excitation to a single, narrow beam of radiation, the origin of the light photons can be inferred regardless of where these photons were detected, and how many times they scattered in tissue. By including an X-ray detector in the system, anatomical imaging is performed simultaneously with molecular imaging via standard X-ray computed tomography. The molecular and anatomical images are spatially and temporally co-registered. Simulations of an XLCT system were performed using an analytical beam model. A preliminary experiment was also conducted using a superficial treatment beam and an EM-CCD camera. **Results:** Tracer uptake in a 2 mm-diameter target can be detected and quantified with sub-picomolar sensitivity using less than 1 cGy of radiation dose, a result that makes XLCT potentially more sensitive than PET, currently one of the most sensitive molecular imaging modalities. Provided sufficient signal-to-noise ratio, the spatial resolution of the system can be made as small as needed by narrowing the beam aperture. In particular, 1 mm uniform spatial resolution was achieved for a 1 mm-wide X-ray beam. Images reconstructed from experimental XLCT measurements showed good agreement with the simulation model.